

# Optical Investigation of ZnO Nanowires

G. MARTÍNEZ-CRIADO<sup>a,\*</sup>, M. HERNÁNDEZ-VÉLEZ<sup>b</sup>, I. LETARD<sup>a</sup>, A. CROS<sup>c</sup>, A. CANTARERO<sup>c</sup>,  
I. MÍNGUEZ-BACHO<sup>b</sup>, J. SUSINI<sup>a</sup>, R. TUCOULOU<sup>a</sup>, J.A. SANS<sup>a</sup>, R. SANZ<sup>b</sup> AND M. VÁZQUEZ<sup>b</sup>

<sup>a</sup>European Synchrotron Radiation Facility, Experiments Division, 38043 Grenoble, France

<sup>b</sup>Materials Science Institute, CSIC-Madrid, 28049 Cantoblanco, Spain

<sup>c</sup>Department of Applied Physics, Valencia University, 46100 Burjassot, Spain

In this study we report the application of synchrotron X-ray fluorescence, photoluminescence and Raman scattering techniques to the analysis of the incorporation of impurities in unintentionally doped ZnO nanowires. Highly ordered one-dimensional ZnO arrays were fabricated by an oxidation process of Zn metal electrodeposited in nanoporous anodic alumina template. X-ray fluorescence data show the contribution of residual elements into the ZnO nanowires growth. A rough analytical quantification of the main light and heavy chemical contents derives impurity concentrations below 1%. The optical efficiency of ZnO nanowires is strongly affected by non-radiative centers up to temperatures as low as 100 K. The photoluminescence was found to be totally dominated by optical transitions associated with the anodic alumina template. Finally, the Raman scattering provides no evidence of local vibrational modes or secondary phases, but it shows the unambiguous signature of the ZnO hexagonal phase.

PACS numbers: 85.75.-d, 61.10.Ht, 78.70.En, 81.05.Ea

## 1. Introduction

Among transparent semiconducting oxides, ZnO is probably the most commonly studied material because of its unique characteristics. With a relatively large exciton binding energy (60 meV) as well as potential piezoelectric and magnetic properties, it crystallizes in the wurtzite structure and has a direct wide band gap of about 3.4 eV at 300 K [1]. In consequence, nowadays it covers a rich variety of nanostructures: highly ordered nanowire arrays, tower-like features, nanorods, nanobelts, nanosprings, nanocombs, nanorings, etc. [2]. Within the framework of crystal growth techniques, electrochemical deposition has been one of the most cost-effective synthesis routes toward the ZnO nanoworld [3]. Different groups have obtained columns on *F*-doped SnO<sub>2</sub> (FTO) substrates, between 100 and 300 nm in diameter, and 400 to 900 nm in height, by varying the electrodeposition parameters (e.g., current density, deposition time, and bath temperature) [4]. Ordered porous ZnO films have been also fabricated by electrodeposition on Sn-doped In-oxide (ITO) glass substrates covered with a polystyrene array template [5]. Besides, Zn nanowires were electrodeposited with diameters of 15–90 nm into porous of the alumina template and oxidized to ZnO in air at 300 °C [3]. However, as in all beginnings, to manipulate their properties, a major concern today is to find experimental conditions under which desired nanostructures present well-

-controlled doping. But, there are experimental difficulties in the unambiguous determination of the signal contamination by residual magnetic particles [6]. So far, the extensive experimental search for multifunctional materials has resulted, for instance, in the development of systems which exhibit surprisingly stable ferromagnetism despite having a small or in some cases nominally zero concentration of magnetic elements [7]. It has been argued that contamination by magnetic nanoparticles accounts for ferromagnetic signatures [8]. Therefore, a large number of basic and systematic studies is still necessary to improve and optimize the current approaches.

In the present work, we apply synchrotron X-ray fluorescence (XRF) to analyze the chemical composition of unintentionally doped ZnO nanowires, electrodeposited in a nanoporous anodic alumina template. The influence of detected elemental traces on the vibrational and optical properties of polycrystalline ZnO nanowires is studied by the Raman scattering and photoluminescence (PL) spectroscopic techniques.

## 2. Experimental details

Nanopore arrays were first patterned with a self-ordered configuration on a high-purity Al substrate (99.999%; Good Fellow) by a two-step anodization process [9]. The arrangement and shape of alumina pores were determined by the applied voltage (40 V), anodization temperature (0–2 °C) and concentration of the electrolyte (H<sub>2</sub>C<sub>2</sub>O<sub>4</sub>, 0.3 M). Figure 1 displays a plane-view micrograph of the as-prepared porous alumina template taken by high-resolution scanning electron microscopy

\* corresponding author; e-mail: [gmartine@esrf.fr](mailto:gmartine@esrf.fr)

(Jeol HRSEM, model JM6400), accompanied with its energy dispersive X-ray (EDX) spectrum. The typical  $K_{\alpha}$  X-ray emission lines of O and Al elements are shown. The template exhibits a perfect two-dimensional array with a well-aligned channel matrix in the nanometer scale. A high-periodicity and uniform close-packed nanoporosity characterize the anodic alumina substrate [10]. The pore diameter and the interpore distance are about 35 and 105 nm, respectively. The average nanopore density is about  $10^{10} \text{ cm}^{-2}$  with a nanopore length of  $5 \mu\text{m}$ . Then, the electrochemical deposition of pure Zn metal in the resulting anodic alumina substrate took place [11], followed by an oxidation process of embedded Zn nanowire arrays in air at  $300 \text{ }^{\circ}\text{C}$  [3] up to obtain polycrystalline ZnO. The electrodeposition process was carried out by applying 30 mA constant current. The aqueous bath contained 0.3 M  $\text{ZnSO}_4 \cdot 7\text{H}_2\text{O}$  and 0.3 M  $\text{H}_3\text{BO}_3$ , and the pH was adjusted to 4.5 by addition of NaOH. The purity of the chemical baths are: zinc sulphate heptahydrated (99.5%; Fluka), manganese (II) chloride tetrahydrated (99%; Fluka), perchloric acid (60% in water solution; Merck), ortho-phosphoric acid (85%; Merck), chromium (VI) oxide (98.5%; Panreac), oxalic acid di-hydrated (99.5%; J.T. Baker), sodium hydroxide (98.0%; Fluka), and boric acid (99.8%; Panreac).

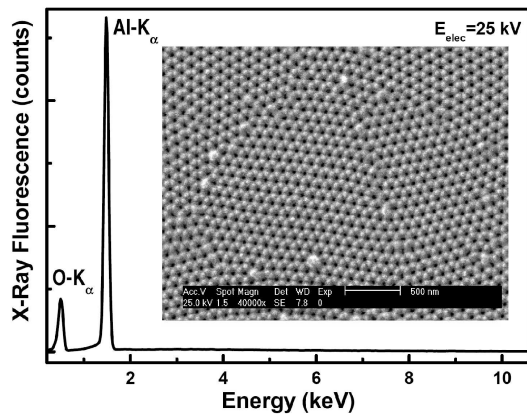


Fig. 1. Energy dispersive X-ray spectrum of the as-prepared anodic alumina substrate accompanied with a high-resolution scanning electron microscopic image. The scale is indicated in the figure.

X-ray microanalyses were performed at the station ID18F of the European Synchrotron Radiation Facility (ESRF) [12]. The beamline is equipped with a three undulators source and a fixed-exit double Si (111) crystal monochromator with an energy resolution of  $\Delta E/E \approx 10^{-4}$ . The monochromatic beam is focused on the sample surface by means of Al compound refractive lenses ( $\approx 10^9$  photons/sec in the focused beam at 14.4 keV). The optical stack uses 56 lenses with parabolic profile and the radius of curvature of  $196 \mu\text{m}$  [13]. The intensity of the incident X-ray beam is monitored with a mini-ionization chamber [14], while a single element solid state Si(Li) detector (150 eV/Mn- $K_{\alpha}$  energy resolution at 4 ms shaping

time;  $30 \text{ mm}^2$  active area; 4 mm active thickness) collects the characteristic X-ray fluorescence lines. By creating a secondary source using the beamline slits ( $0.1 \times 0.1 \text{ mm}$ ), the beam dimensions estimated by the Au knife-edge scan method [15] are  $1.9 \times 2.4 \mu\text{m}^2$  ( $V \times H$ ) at 14.4 keV.

On the other hand, the Raman scattering and photoluminescence measurements were carried out using a Jobin-Yvon T64000 triple spectrometer equipped with a confocal OLYMPUS microscope and a nitrogen-cooled open electrode charge-coupled device (CCD) detector. Several lines of the SABRE  $\text{Ar}^+$  laser, comprising a wide wavelength range from 514.5 nm to 351.1 nm, as well as a doubled  $\text{Ar}^+$  laser beam (244 nm) are used as excitation sources. With  $100\times$  and  $40\times$  objectives, the diameter of the laser spot is  $1 \mu\text{m}$  and  $4 \mu\text{m}$  for visible and ultraviolet laser excitation, respectively. The Raman spectra are collected at room temperature in backscattering geometry with a spectral resolution of about  $1 \text{ cm}^{-1}$ . A liquid nitrogen micro-cryostat (CryoVac GmbH & Co KG) allows the low-temperature PL measurements.

### 3. Results and discussion

In order to study the incorporation of chemical species during the crystal growth, XRF analysis is carried out using the synchrotron radiation microbeam as an excitation source. In general, by EDX microanalysis, the major elements are quantitatively determined [16]. However, the accurate knowledge of the minor elemental composition down to trace concentration levels can not be identified unambiguously by this technique because of the bremsstrahlung radiation that restricts the detection limit. By synchrotron XRF, on the contrary, very low and multi-elemental densities can be detected at the micrometer scale [17]. The spectra are recorded at an incident angle  $\theta = 45 \pm 5^{\circ}$  with respect to the surface of the sample. Figure 2 shows the typical XRF signals of ZnO nanowires and of the alumina template. The ZnO spectrum consists of a well-defined background on which sharp characteristic lines and spectral artifacts are superimposed. The  $K_{\alpha}$  and  $K_{\beta}$  fluorescence lines of Zn, as well as Ar from the air, are shown for 14.4 keV excitation energy. The escape peak generated from the Si(Li) solid state detector at 1.74 keV (Si  $K_{\alpha}$  energy) from the Zn parent line is also indicated. Taking only the peak-like structures statistically significant, the presence of several species is revealed in the considered energy range: Ca, Cr, Mn, Fe, Ni, Cu, Ga, and As. Such elements may originate from residual impurities in the growth chamber (memory effects) or source materials, as well as, they being introduced by growth processing procedures. Since almost no traces were identified from the XRF signal of the anodic alumina template, in principle, the chemical pre-treatments of the Al sheet (99.997% pure), as well as, its subsequent two-step anodization process could be ruled out. Thus, the control of background impurities might depend fundamentally on the Zn electrodeposition and further oxidation step. As a

matter of fact, we believe that mostly the electrochemical system (electrolytic bath and metallic sources) plays the key role in the observed contamination. In general, the detected heavy transition elements could affect both the incorporation and agglomeration stages of microdefect formation, being crucial particularly in the magnetic properties. It has been shown that uncompensated spins in antiferromagnetic nanoparticles could produce additional sizeable spontaneous magnetization at high temperatures [18]. From the peak intensities, assuming an incident monochromatic beam on a flat sample without secondary excitation, a rough quantitative analysis using PyMCA code [19] yielded residual concentrations ranging from: 0.9% Ca, 0.07% Ga, 0.06% Cr, 0.05% Ni, up to 0.04% Fe. In contrast to previous results obtained by EDX, which pointed out that samples grown without an applied potential in the electrochemical deposition contained no measurable dopants [20], our findings by XRF show nonnegligible improper handling and/or source contamination with a detectable overall elemental contribution into the fabrication processes.

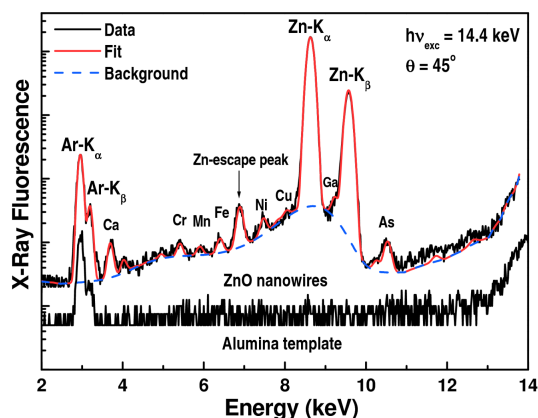


Fig. 2. X-ray fluorescence spectra of ZnO nanowires and of the anodic alumina substrate recorded with an excitation energy of 14.4 keV.

The statements above are supported by the PL studies. In Fig. 3 the luminescence spectra taken at room temperature are plotted. Usually, the radiative recombination of ZnO nanostructures consists of two dominant bands: a low energy (green) transition associated with emissions from deep levels caused by structural defects, and a high energy (ultraviolet) line mostly attributed to near-band edge emissions, namely excitonic recombinations [21]. So far, the former transition has been associated with different origins: singly ionized oxygen vacancy [22], antisite oxygen [23] or donor-acceptor complexes [24]. However, unlike the typical PL, here the ZnO luminescence signal is totally quenched and the spectra are basically dominated all over the sample by the emission bands coming from the nanoporous anodic alumina substrate. Accordingly, our results indicate that the optical efficiency of ZnO nanowires is determined by nonradiative centers. Consistently with the residual doping levels found by XRF

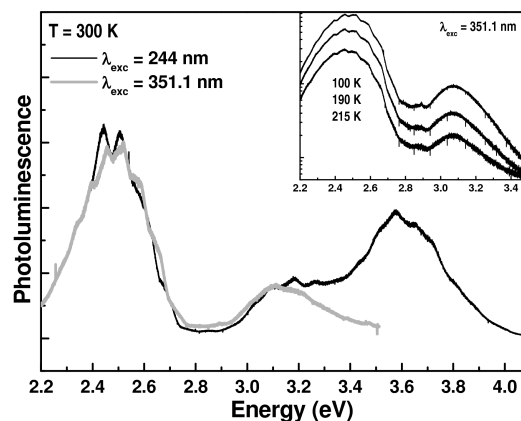


Fig. 3. Room temperature photoluminescence spectra of ZnO nanowires electrodeposited on the anodic alumina substrate, recorded with two different excitation wavelengths: 244 nm and 351.1 nm. The inset shows the measured spectrum at different temperatures.

microanalysis, additional processes influence the decay of the luminescence efficiency, such as trapping at impurities and/or defects, Auger or surface/interface recombinations, etc. It is well-known that local fields produced by such defects, as well as, fluctuations of the location of atoms in the crystal induce the exciton dissociation, making the excitonic transitions undetectable. For the porous anodic alumina substrate, on the contrary, three bands are located at 2.5 eV, 3.1 eV, and 3.6 eV depending on the excitation wavelengths. Up to now, the PL nature of different emissions is still ambiguous though most of reports have tentatively attributed them to  $F^+$  and  $F$  centers, related to oxygen vacancy defects, as well as, to oxalic impurities (especially light elements) [25, 26]. Small superimposed oscillations that appear on the PL curves could be associated with interference effects like Huang et al. recently published [27]. In contrast to  $\gamma$ -alumina nanoparticles [28], here under ultraviolet excitation ( $\lambda_{exc} = 244$  nm with a power density of  $10^3$  W/cm<sup>2</sup>) there is no induced degradation in the PL intensity of low energy bands. Moreover, it was found that peak positions and full-widths at half maximum of the main PL bands do not depend on thermal conditions (see inset in Fig. 3). Furthermore, the small spot size reveals that there is no significant inhomogeneity, illustrating a uniform projection of different electron-hole recombination channels over the template, at least within the detectable lateral resolution.

In order to confirm that the major elements were incorporated into the crystalline structure, Raman scattering measurements were performed. Since ZnO crystallizes in the wurtzite structure belong to the  $C_{6v}^4$  ( $P6_3mc$ ) space group, the zone center phonons are:  $2A_1 + 2B_1 + 2E_1 + 2E_2$ , from which one  $A_1$ , one  $E_1$ , and two  $E_2$  are Raman active, whereas  $B_1$  modes are silent. In addition, one set of  $A_1$  and  $E_1$  corresponds to acoustic phonons. The anisotropic short-range order of the hexagonal structure

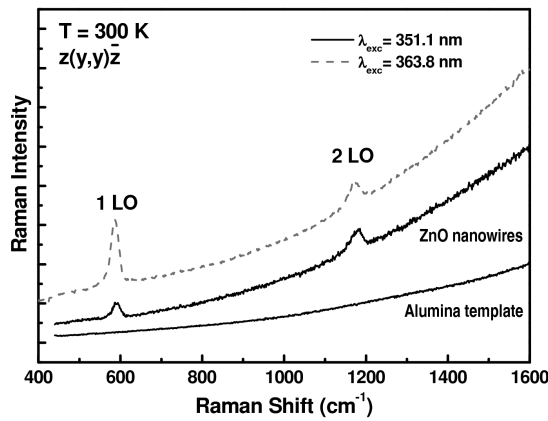


Fig. 4. Room temperature Raman spectra of ZnO nanowires and of the anodic alumina substrate taken in backscattering geometry. The spectra were recorded with 351.1 nm and 363.8 nm lines of the Ar<sup>+</sup> laser.

is responsible for the  $A_1 - E_1$  splitting, whereas the long-range Coulomb field causes the polar modes split into longitudinal — transverse optical (LO — TO) modes at the zone center. Figure 4 shows the typical Raman spectrum of ZnO nanowires, where two major bands are centered at  $577\text{ cm}^{-1}$  and  $1152\text{ cm}^{-1}$ , with bandwidths at  $30\text{ cm}^{-1}$  and  $46\text{ cm}^{-1}$ , respectively. Under backscattering configuration  $z(y,y)\bar{z}$  ( $z \parallel c$  axis), both phonon modes  $E_2$  and  $A_1(\text{LO})$  are allowed by Raman selection rules. However, when the sample is excited in the visible region (514.5 nm, 488.0 nm, not shown), the spectra are dominated by modes from the alumina template. On the other hand, for excitation closer to the bandgap (363.8 nm, 351.1 nm, shown in Fig. 4), that is near resonant conditions, an enhancement of the polar  $A_1(\text{LO})$  mode due to Fröhlich electron-phonon scattering is expected. In consequence, the bands shown in Fig. 4 are attributed to the Raman  $A_1(\text{LO})$  phonon scattering and its corresponding overtones. No disorder-induced modes due to vacancies [29] or local vibrational modes at transition metal impurities [30, 31] are displayed in the figure. Moreover, in the considered frequency range the Raman spectra exhibit no secondary phases or further additional modes specific for residual dopants. Without background subtraction and under near resonant conditions, the enhancement of the multi-LO phonon scattering of the ZnO nanowires is clearly observed when comparing 363.8 nm and 351.1 nm excitations. Up to now, multiphonon scattering processes have been previously reported for several low-dimensional ZnO systems [32–34].

#### 4. Conclusions

Hexagonal ZnO have been synthesized in the nanoporous anodic alumina template. The elemental composition has been identified and estimated by synchrotron XRF analysis. Impurity contaminations of electrodeposited nanostructures have been revealed at low

concentration levels. These residual impurities could be partially responsible for the non-radiative processes that dominate the PL of ZnO nanowires. The overall electron-hole recombination was characterized by intense emission bands from the alumina template and it was attributed to different point defects. The Raman spectra did not exhibit additional phonon modes, except the multiple LO phonon peaks observed under near resonant conditions.

#### Acknowledgments

The authors are thankful to the Spanish Ministry of Science and Technology and the Generalitat Valenciana for the financial support. Special thanks are due to Sylvain Laboure for his useful help.

#### References

- [1] Ü. Özgür, Ya.I. Alivov, C. Liu, A. Teke, M.A. Reshchikov, S. Dogan, V. Avrutin, S.-J. Cho, H. Morkoç, *J. Appl. Phys.* **98**, 041301 (2005).
- [2] L. Schmidt-Mendea, J.L. MacManus-Driscolla, *Materials Today* **10**, 40 (2007).
- [3] Y. Li, G.W. Meng, L.D. Zhang, F. Phillipp, *Appl. Phys. Lett.* **76**, 2011 (2000).
- [4] J. Cembrero, A. Elmanouni, B. Hartiti, M. Mollar, B. Mari, *Thin Solid Films* **451-452**, 198 (2004).
- [5] Z.F. Liu, Z.G. Jin, J.J. Qiu, X.X. Liu, W.B. Wu, W. Li, *Semicond. Sci. Technol.* **21**, 60 (2006).
- [6] T. Dietl, *J. Phys., Condens. Matter* **19**, 165204 (2007).
- [7] S. Kuroda, N. Nishizawa, K. Takita, M. Mitome, Y. Bando, K. Osuch, T. Dietl, *Nature Materials* **6**, 440 (2007).
- [8] J. Philip, A. Punnoose, B.I. Kim, K.M. Reddy, S. Layne, J.O. Holmes, B. Satpati, P.R. Leclair, T.S. Santos, J.S. Moodera, *Nature Materials* **5**, 298 (2006).
- [9] H. Masuda, K. Fukuda, *Science* **268**, 1466 (1995).
- [10] M. Vázquez, K. Nielsch, P. Vargas, J. Velazquez, D. Navas, K. Pirola, M. Hernandez-Velez, E. Vogel, J. Cartes, R.B. Wehrspohn, U. Gosele, *Physica B* **343**, 395 (2004).
- [11] M. Hernández-Vélez, *Thin Solid Films* **495**, 51 (2006).
- [12] A. Somogyi, M. Drakopoulos, L. Vincze, B. Veke-mans, C. Camerani, K. Janssens, A. Snigirev, F. Adams, *X-ray Spectrometry* **30**, 242 (2001).
- [13] B. Lengeler, C. Schroer, J. Tümmeler, B. Benner, M. Richwin, A. Snigirev, I. Snigireva, M. Drakopoulos, *J. Synchrotron Rad.* **6**, 1153 (1999).
- [14] M.K.M. Kocsis, A. Somogyi, *J. Synchrotron Rad.* **10**, 187 (2003).
- [15] G. Martínez-Criado, A. Somogyi, S. Ramos, J. Campo, R. Tucoulou, M. Salome, J. Susini, M. Hermann, M. Eickhoff, M. Stutzmann, *Appl. Phys. Lett.* **86**, 131927 (2005).

- [16] *Handbook of X-Ray Spectrometry*, Practical Spectroscopy Series 29, Ed. R.E. Van Grieken, A.A. Markowicz, Dekker, New York 2002.
- [17] *Microscopic X-Ray Fluorescence Analysis*, Ed. K.H.A. Janssens, F.C.V. Adams, A. Rindby (2000).
- [18] E. Winkler, R.D. Zysler, M. Vasquez-Mansilla, D. Fiorani, *Phys. Rev. B* **72**, 132409 (2005).
- [19] V.A. Solé, E. Papillon, M. Cotte, Ph. Walter, J. Susini, *Spectrochimica Acta Part B* **62**, 63 (2007).
- [20] J.B. Cui, U.J. Gibson, *Appl. Phys. Lett.* **87**, 133108 (2005).
- [21] B.D. Yao, Y.F. Chan, N. Wanga, *Appl. Phys. Lett.* **81**, 757 (2002).
- [22] K. Vanheusden, W.L. Warren, C.H. Seager, D.R. Talant, J.A. Voigt, B.E. Gnade, *J. Appl. Phys.* **79**, 7983 (1996).
- [23] B. Lin, Z. Fu, Y. Jia, *Appl. Phys. Lett.* **79**, 943 (2001).
- [24] S.A. Studenikin, M. Cocivera, *J. Appl. Phys.* **91**, 5060 (2002).
- [25] Z. Li, K. Huang, *J. Phys., Condens. Matter* **19**, 216203 (2007).
- [26] W.L. Xu, M.J. Zheng, S. Wu, W.Z. Shen, *Appl. Phys. Lett.* **85**, 4364 (2004).
- [27] K. Huang, L. Pu, Y. Shi, P. Han, R. Zhang, Y.D. Zheng, *Appl. Phys. Lett.* **89**, 201118 (2006).
- [28] S. Liu, L. Zhang, Y. Fan, J. Luo, P. Zhang, L. An, *Appl. Phys. Lett.* **89**, 051911 (2006).
- [29] W. Gebicki, K. Osuch, C. Jastrzebski, Z. Golacki, M. Godlewski, *Superlatt. Micr.* **38**, 428 (2005).
- [30] J. Yu, H. Xing, Q. Zhao, H. Mao, Y. Shen, J. Wang, Z. Lai, Z. Zhu, *Sol. Stat. Commun.* **38**, 502 (2006).
- [31] C. Bundesmann, N. Ashkenov, M. Schubert, D. Spemann, T. Butz, E.M. Kaidashev, M. Lorenz, M. Grundmann, *Appl. Phys. Lett.* **83**, 1974 (2003).
- [32] H.T. Ng, B. Chen, J. Li, J. Han, M. Meyyappan, J. Wu, S.X. Li, E.E. Haller, *Appl. Phys. Lett.* **82**, 2023 (2003).
- [33] V.V. Ursaki, I.M. Tiginyanu, V.V. Zalamai, E.V. Rusu, G.A. Emelchenko, V.M. Masalov, E.N. Samarov, *Phys. Rev. B* **70**, 155204 (2004).
- [34] B. Kumar, H. Gong, S.Y. Chow, S. Tripathy, Y. Hua, *Appl. Phys. Lett.* **89**, 071922 (2006).